Two-dimensional finite-difference model of seafloor compliance

P. Iassonov, W.C. Crawford

Geophys. J. Int. (2008) **174,** 525–541 doi: 10.1111/j.1365-246X.2008.03782.x

Two-dimensional finite-difference model of seafloor compliance

Pavel Iassonov[1] and Wayne Crawford[2]

[1] *University of Arizona, Department of Soil, Water and Environmental Science.* 502 *Shantz Building, Tucson, AZ,* 85721*, USA.*
E-mail: iassonov@email.arizona.edu
[2] *Institut de Physique du Globe de Paris, Laboratoire de Géosciences Marines. Case* 89*, Tour* 14-15*,* 4 *Place Jussieu,* 75252*, Paris, France*

Accepted 2008 March 6. Received 2008 February 12; in original form 2007 April 9

SUMMARY

Seafloor compliance is the measure of seafloor deformation under a pressure signal. Our new 2-D finite-difference compliance modelling algorithm presents several advantages over the existing compliance models, including the ability to handle any gridded subsurface structure with no limitations on the gradients of the material properties, as well as significantly improved performance. Applying this method to some of the problems inaccessible to previously existing methods, demonstrates that lateral variations in subsurface structure must be accounted for to adequately interpret compliance data. In areas with significant lateral variations, the utilization of 1-D modelling and inversion is likely to result in high interpretation errors, even when additional subsurface structure information is available. We find that flattened pure melt bodies have a significantly higher compliance than cylindrical melt bodies with the same cross-sectional area. The compliance created by such bodies often has side peaks over their edges, which are as strong as or stronger than the central peak, requiring a series of measurements to best constrain their size and shear velocity. Finally, we find that the compliance data are far and away most sensitive to the broad, thick, lower-crustal partial melt zone. Our simple data fitting model for the compliance measurements on the East Pacific Rise at 9°48′N required shear velocities as low as 700 ms^{-1} in the centre of this zone, far below the values previously estimated using 1-D modelbased inversions, suggesting higher melt percentages than those previously estimated, while small melt bodies in the upper part of the crust were found to have little or no effect on the measured compliance.

Key words: Fourier analysis; Numerical approximations and analysis; Composition of the oceanic crust; Mid-ocean ridge processes; Magma genesis and partial melting; Pacific Ocean.

1 INTRODUCTION

Seafloor compliance is the deformation of the seafloor under a pressure signal. More specifically, the compliance (sometimes referred to as normalized compliance) is the transfer function between the seafloor vertical displacement $u_z(\omega)$ and the pressure $\tau_{zz}(\omega)$ at the seabed, multiplied by the forcing wavenumber $k(\omega)$ at a given frequency ω:

$$\eta(\omega) = k(\omega)\,\frac{u_z(\omega)}{\tau_{zz}(\omega)}. \tag{1}$$

The compliance is sensitive to the subsurface shear modulus and particularly to low shear modulus zones such as melt bodies and porous sediments (Yamamoto & Torii 1986; Yamamoto *et al.* 1989; Crawford *et al.* 1991, 1998; Hulme *et al.* 2003, 2005; Latychev & Edwards 2003). Compliance measurements have been used to constrain sediment velocities (Trevorrow & Yamamoto 1991; Crawford & Singh 2006), to study melt beneath oceanic spreading centres (Crawford *et al.* 1991, 1999; Crawford 1994; Crawford & Webb 2002) and to evaluate gas hydrates (Willoughby & Edwards 1997, 2000). Compliance measurements on the East Pacific Rise (EPR) between 9°N and 10°N reveal a broad zone of partial melt within the lower crust, which is centred near the rise axis underlain in places by zones of enhanced melt at or near the Moho (Crawford *et al.* 1998; Crawford & Webb 2002). The compliance changes rapidly off axis and varies along axis over the Moho melt bodies and, to a lesser extent, the lower crustal mush zone, indicating significant lateral variations in the subsurface melt content. The East Pacific Rise (EPR) is one of the morphologically most uniform ocean ridges, suggesting that other mid-ocean ridges should have even more complex melt systems (Phipps Morgan 1987; Smith & Cann 1993; Cannat 1996, 1998; Buck *et al.* 1997). Lateral variations in fluid-filled bodies are also important in other scientific and commercial problems, including studies of the magma plumbing beneath interplate volcanoes, the extent of hydrothermal circulation zones and the identification and monitoring of petroleum reservoirs.

To properly constrain the subsurface melt distribution using compliance measurements, we must be able to correctly forward model the seafloor compliance over regions with strong spatial shear velocity gradients. Currently, compliance is most often modelled using a 1-D matrix propagator code, which, although very fast, cannot model compliance over 2-D fluid bodies and breaks down for very low shear moduli (Gomberg & Masters 1988; Crawford *et al.* 1991). Crawford *et al.* (1998) developped a 2-D finite-difference code to model compliance, but that code could not model sudden changes in material properties. Latychev & Edwards (2003) developed a 3-D compliance modelling finite-difference code using control volumes, but their method makes certain assumptions (geometrical averaging of the material properties, quasi-static solution only) that may invalidate results for materials with low shear moduli. Hulme *et al.* (2005) developed a quasi-analytic solution for a fluid (or other) cylinder buried in a uniform medium, using scattering theory. Although limited to one geometry, this model provided the surprising result that a 'mush' cylinder (shear velocity = 1.5 km s^{-1}) had nearly the compliance signal as a pure melt cylinder (shear velocity = 0 km s^{-1}), which is very different from the 1-D case where the compliance peak height increases nearly as the inverse of the shear modulus.

We present here a new compliance modelling code using finite differences and control elements, which is capable of calculating the seafloor compliance over any gridded subsurface model, including embedded fluid bodies of arbitrary shape and size. We use this model to investigate the sensitivity of compliance to different types of fluid bodies that could not previously be modelled, including the sensitivity of seafloor compliance to melt/mush lenses versus melt/mush cylinders, and the effective velocity of melt zones composed of several melt lenses that are too small to be resolved individually. We also investigate the narrow-band compliance peaks that have been measured at several East Pacific Rise (EPR) sites, and which have been interpreted as narrow melt bodies near the Moho (Crawford *et al.* 1999; Crawford & Webb 2002).

2 THE MODEL

2.1 Basic equations

We use a 2-D model in this paper. Although extension of the model to 3-D would be trivial, the memory requirements and calculation times for models of similar resolution would increase beyond what our available computational resources could handle. Our early tests have shown that the decrease in spatial resolution required to bring the model memory requirements to acceptable levels (below 4Gb) would result in unacceptably high computational errors. Another memory-saving alternative would be to use an iterative solution method; however, we were unable to find an iterative scheme that would provide reasonable convergence speed in all cases, as will be explained later in this section.

The 2-D equations of motion for an elastic solid can be written as (Aki & Richards 1980):

$$\rho \frac{\partial^2 u}{\partial t^2} = \frac{\partial \tau_{xx}}{\partial x} + \frac{\partial \tau_{xz}}{\partial z},$$
$$\rho \frac{\partial^2 w}{\partial t^2} = \frac{\partial \tau_{zz}}{\partial z} + \frac{\partial \tau_{zx}}{\partial x}, \tag{2}$$

where u and w are horizontal and vertical components of the displacement vector, respectively, and the stress tensor components τ_{ij} are:

$$\tau_{xx} = (\lambda + 2\mu) \frac{\partial u}{\partial x} + \lambda \frac{\partial w}{\partial z},$$
$$\tau_{zz} = (\lambda + 2\mu) \frac{\partial w}{\partial z} + \lambda \frac{\partial u}{\partial x},$$
$$\tau_{xz} = \tau_{zx} = \mu \left(\frac{\partial u}{\partial z} + \frac{\partial w}{\partial x} \right), \tag{3}$$

where λ and μ are the Lamé parameters (Aki & Richards 1980).

The boundary conditions for the compliance problem are free slip of the seabed:

$$\tau_{xz}|_{z=Z} = 0, \tag{4}$$

where Z is the z-coordinate of the seabed and the plane wave pressure forcing

$$\tau_{zz}|_{z=Z} = P(x,t) = P_0 e^{i(\omega t - kx)}, \tag{5}$$

where P_0 is the amplitude of the pressure oscillations (Crawford *et al.* 1991). We thus look for the solution in the frequency domain, so,

$$\frac{\partial^2 u}{\partial t^2} = -\omega^2 u, \quad \frac{\partial^2 w}{\partial t^2} = -\omega^2 w. \tag{6}$$

2.2 Finite-difference approximation

Our computation domain is a rectilinear grid defined by two sets of coordinates x_i and z_j, where $i = \{1, N\}$ and $j = \{1, M\}$; the set of indices (i, j) uniquely represents all 'nodes' of the grid. We further postulate that the material properties (bulk density and the Lamé parameters) are constant within each grid 'cell' (Fig. 1), and that ρ_{ij}, λ_{ij} and μ_{ij} represent the values of the bulk density and Lamé parameters in the grid cell located to the upper right-hand side of the node (i, j) (Fig. 1).

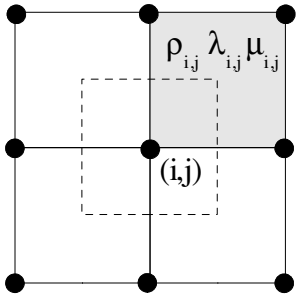

Figure 1. Illustration of grid structure and material properties distribution. Dashed line indicates the control element used in calculations.

The main reason for choosing this discretization over the more common approach of assuming linear variation of material properties between the adjacent nodes of the grid is that it allows us to define arbitrarily sharp boundaries within the model, which is important for representation of features such as melt lenses within the constrains of limited grid resolution. Combined with subsequent integration of the governing equations, this approach circumvents direct calculation or estimation of the derivatives of the material properties, thus avoiding associated errors. In contrast, the ordinary finite-difference discretization of (2) would be highly sensitive to sharp variations of material properties (Crawford *et al.* 1998) and require significantly higher grid resolution to approach the precision of our method.

To obtain the finite-difference representation of our problem at the node (i, j), we first integrate the equations of motion over the 'control element' defined as:

$$\begin{aligned} &x \in \left\{x_{i-\frac{1}{2}}, x_{i+\frac{1}{2}}\right\}, \quad z \in \left\{z_{j-\frac{1}{2}}, z_{j+\frac{1}{2}}\right\}, \quad \text{where} \\ &x_{i\pm\frac{1}{2}} = \frac{1}{2}\left(x_{i\pm1} + x_i\right), \quad \text{and} \quad z_{j\pm\frac{1}{2}} = \frac{1}{2}(z_{j\pm1} + z_j). \end{aligned} \tag{7}$$

Considering (6) and using the notation (7), the equation of motion (2) can be expressed as:

$$\begin{aligned} -\omega^2 \int_{z_{j-\frac{1}{2}}}^{z_{j+\frac{1}{2}}} \int_{x_{i-\frac{1}{2}}}^{x_{i+\frac{1}{2}}} \rho\, u \,\mathrm{d}x \,\mathrm{d}z &= \int_{z_{j-\frac{1}{2}}}^{z_{j+\frac{1}{2}}} \tau_{xx}\Big|_{x_{i-\frac{1}{2}}}^{x_{i+\frac{1}{2}}} \mathrm{d}z + \int_{x_{i-\frac{1}{2}}}^{x_{i+\frac{1}{2}}} \tau_{xz}\Big|_{z_{j-\frac{1}{2}}}^{z_{j+\frac{1}{2}}} \mathrm{d}x\,, \\ -\omega^2 \int_{z_{j-\frac{1}{2}}}^{z_{j+\frac{1}{2}}} \int_{x_{i-\frac{1}{2}}}^{x_{i+\frac{1}{2}}} \rho\, w \,\mathrm{d}x \,\mathrm{d}z &= \int_{x_{j-\frac{1}{2}}}^{x_{j+\frac{1}{2}}} \tau_{zz}\Big|_{z_{i-\frac{1}{2}}}^{z_{i+\frac{1}{2}}} \mathrm{d}x + \int_{z_{i-\frac{1}{2}}}^{z_{i+\frac{1}{2}}} \tau_{xz}\Big|_{x_{j-\frac{1}{2}}}^{x_{j+\frac{1}{2}}} \mathrm{d}z\,. \end{aligned} \tag{8}$$

We will first calculate the last integral in the right-hand side of the eq. (8). Considering that the values of material properties are constant within each grid cell, we can write

$$\begin{aligned} \int_{x_{i-\frac{1}{2}}}^{x_{i+\frac{1}{2}}} \left\{\mu \frac{\partial w}{\partial x}\right\}\Big|_{z_{j-\frac{1}{2}}}^{z_{j+\frac{1}{2}}} \mathrm{d}x &= \mu_{i-1,j} \int_{x_{i-\frac{1}{2}}}^{x_i} \left.\frac{\partial w}{\partial x}\right|_{z_{j+\frac{1}{2}}} \mathrm{d}x - \mu_{i-1,j-1} \int_{x_{i-\frac{1}{2}}}^{x_i} \left.\frac{\partial w}{\partial x}\right|_{z_{j-\frac{1}{2}}} \mathrm{d}x \\ &+ \mu_{i,j} \int_{x_i}^{x_{i+\frac{1}{2}}} \left.\frac{\partial w}{\partial x}\right|_{z_{j+\frac{1}{2}}} \mathrm{d}x - \mu_{i,j-1} \int_{x_i}^{x_{i+\frac{1}{2}}} \left.\frac{\partial w}{\partial x}\right|_{z_{j-\frac{1}{2}}} \mathrm{d}x. \end{aligned} \tag{9}$$

Each integral in (9) is trivial to calculate. For example,

$$\mu_{i,j-1} \int_{x_i}^{x_{i+\frac{1}{2}}} \left.\frac{\partial w}{\partial x}\right|_{z_{j-\frac{1}{2}}} \mathrm{d}x = \mu_{i,j-1} w\Big|_{x_i, z_{j-\frac{1}{2}}}^{x_{i+\frac{1}{2}}, z_{j-\frac{1}{2}}} = \mu_{i,j-1}\left(w_{i+\frac{1}{2},j-\frac{1}{2}} - w_{i,j-\frac{1}{2}}\right). \tag{10}$$

Considering that the displacement is a continuous function of the coordinates, and that it is a smooth function within each grid cell, the values $w_{i+\frac{1}{2},j-\frac{1}{2}}$ and $w_{i,j-\frac{1}{2}}$ can be approximated by simple linear averaging:

$$w_{i+\frac{1}{2},j-\frac{1}{2}} = \frac{1}{4}(w_{i,j} + w_{i+1,j} + w_{i+1,j-1} + w_{i,j-1}) + O\left(h_x^2\right) + O\left(h_z^2\right) \quad \text{and} \quad w_{i,j-\frac{1}{2}} = \frac{1}{2}(w_{i,j} + w_{i,j-1}) + O\left(h_z^2\right), \tag{11}$$

where

$$\begin{aligned} &h_x = x_{i+1} - x_i \quad \text{and} \\ &h_z = z_{j+1} - z_j, \end{aligned} \tag{12}$$

are the horizontal and vertical sizes of the particular grid cell, respectively. The following notation will also be used in later calculations.

$$\begin{aligned} &h_x^- = x_i - x_{i-1}, \quad \text{and} \\ &h_z^- = z_j - z_{j-1}. \end{aligned} \tag{13}$$

The rest of the finite-difference representation of (9) can be obtained in the similar manner. The resulting expression is

$$\int_{x_{i-\frac{1}{2}}}^{x_{i+\frac{1}{2}}} \left\{\mu \frac{\partial w}{\partial x}\right\}\Big|_{z_{j-\frac{1}{2}}}^{z_{j+\frac{1}{2}}} \mathrm{d}x = \frac{1}{4}\Big[w_{i,j}(\mu_{i,j-1} + \mu_{i-1,j} - \mu_{i,j} - \mu_{i-1,j-1}) + w_{i+1,j}(\mu_{i,j} - \mu_{i,j-1}) + w_{i-1,j}(\mu_{i-1,j-1} - \mu_{i-1,j}) + w_{i,j+1}(\mu_{i-1,j} - \mu_{i,j}) + w_{i,j-1}(\mu_{i,j-1} - \mu_{i-1,j-1}) + w_{i+1,j+1}\mu_{i,j} + w_{i+1,j-1}\mu_{i,j-1} + w_{i-1,j+1}\mu_{i-1,j} + w_{i-1,j-1}\mu_{i-1,j-1}\Big]. \quad (14)$$

The calculations for the next type of integral are slightly different, but proceed in the similar way:

$$\int_{x_{i-\frac{1}{2}}}^{x_{i+\frac{1}{2}}} \left\{\mu \frac{\partial u}{\partial z}\right\}\Big|_{z_{j-\frac{1}{2}}}^{z_{j+\frac{1}{2}}} \mathrm{d}x = \mu_{i-1,j}\int_{x_{i-\frac{1}{2}}}^{x_i} \frac{\partial u}{\partial z}\Big|_{z_{j+\frac{1}{2}}} \mathrm{d}x - \mu_{i-1,j-1}\int_{x_{i-\frac{1}{2}}}^{x_i} \frac{\partial u}{\partial z}\Big|_{z_{j-\frac{1}{2}}} \mathrm{d}x + \mu_{i,j}\int_{x_i}^{x_{i+\frac{1}{2}}} \frac{\partial u}{\partial z}\Big|_{z_{j+\frac{1}{2}}} \mathrm{d}x - \mu_{i,j-1}\int_{x_i}^{x_{i+\frac{1}{2}}} \frac{\partial u}{\partial z}\Big|_{z_{j-\frac{1}{2}}} \mathrm{d}x. \quad (15)$$

The first-order derivatives in (15) can be discretized using standard centred finite-difference scheme, for example,

$$\frac{\partial u}{\partial z}\Big|_{z_{j+\frac{1}{2}}} = \frac{u_{x,j+1} - u_{x,j}}{h_z} + O\left(h_z^2\right) \quad \text{and} \quad \frac{\partial u}{\partial z}\Big|_{z_{j-\frac{1}{2}}} = \frac{u_{x,j} - u_{x,j-1}}{\left(h_z^-\right)} + O\left(\left(h_z^-\right)^2\right). \quad (16)$$

Here we use mixed notation of type $u_{x,j}$ to indicate that at this stage in derivation, although the z is discretized, the x is still considered a continuous variable.

Integrals in the right-hand side of (15) can now be discretized using (16) and Taylor expansion series to the second order. For example,

$$\begin{aligned}\mu_{i,j}\int_{x_i}^{x_{i+\frac{1}{2}}} \frac{\partial u}{\partial z}\Big|_{z_{j+\frac{1}{2}}} \mathrm{d}x &= \mu_{i,j}\int_{x_i}^{x_{i+\frac{1}{2}}} \left[\frac{1}{h_z}(u_{x,j+1} - u_{x,j}) + O\left(h_z^2\right)\right]\mathrm{d}x \\ &= \frac{\mu_{i,j}}{h_z}\left[\frac{h_x}{2}u_{i,j+1} + \frac{h_x}{2}(u_{i+1,j+1} - u_{i,j+1}) - \frac{h_x}{2}u_{i,j} - \frac{h_x}{2}(u_{i+1,j} - u_{i,j}) + O\left(h_x^3\right)\right] + O(h_z h_x) \\ &= \frac{1}{8}\mu_{i,j}\frac{h_x}{h_z}[3u_{i,j+1} + u_{i+1,j+1} - 3u_{i,j} - u_{i+1,j}] + O(h_z h_x) + O\left(h_x^3 h_z^{-1}\right). \end{aligned} \quad (17)$$

Applying this method to the rest of (15), we obtain

$$\begin{aligned}\int_{x_{i-\frac{1}{2}}}^{x_{i+\frac{1}{2}}} \left\{\mu \frac{\partial u}{\partial z}\right\}\Big|_{z_{j-\frac{1}{2}}}^{z_{j+\frac{1}{2}}} \mathrm{d}x \approx \frac{1}{8}\Big[&- 3u_{i,j}\left(\mu_{i,j}\frac{h_x}{h_z} + \mu_{i,j-1}\frac{h_x}{h_z^-} + \mu_{i-1,j}\frac{h_x^-}{h_z} + \mu_{i-1,j-1}\frac{h_x^-}{h_z^-}\right) \\ &- u_{i+1,j}h_x\left(\frac{\mu_{i,j}}{h_z} + \frac{\mu_{i,j-1}}{h_z^-}\right) - u_{i-1,j}h_x^-\left(\frac{\mu_{i-1,j}}{h_z} + \frac{\mu_{i-1,j-1}}{h_z^-}\right) + \frac{3}{8}u_{i,j+1}h_z\left(\frac{\mu_{i,j}}{h_x} + \frac{\mu_{i-1,j}}{h_x^-}\right) \\ &+ \frac{3}{8}u_{i,j-1}h_z^-\left(\frac{\mu_{i,j-1}}{h_x} + \frac{\mu_{i-1,j-1}}{h_x^-}\right) + u_{i+1,j+1}\mu_{i,j}\frac{h_x}{h_z} + u_{i+1,j-1}\mu_{i,j-1}\frac{h_x}{h_z^-} + \\ &+ u_{i-1,j+1}\mu_{i-1,j}\frac{h_x^-}{h_z} + u_{i-1,j-1}\mu_{i-1,j-1}\frac{h_x^-}{h_z^-}\Big]. \end{aligned} \quad (18)$$

The other two integrals in the right-hand side of the (8) are of the same types as those already addressed, so, their finite-difference approximation can be obtained from (14) and (18) by simply exchanging the coordinate indices and replacing the material property variable.

We approximate the integral in the left-hand side of the eq. (8) using the same method applied to obtain (18). The resulting expression is

$$\begin{aligned}-\omega^2\int_{z_{j-\frac{1}{2}}}^{z_{j+\frac{1}{2}}}\int_{x_{i-\frac{1}{2}}}^{x_{i+\frac{1}{2}}} \rho\, u\, \mathrm{d}x\, \mathrm{d}z &= \frac{1}{4}\omega^2\left\{u_{i,j}\left(\rho_{i,j}h_x h_z + \rho_{i-1,j}h_x^- h_z + \rho_{i,j-1}h_x h_z^- + \rho_{i-1,j-1}h_x^- h_z^-\right)\right. \\ &+ \frac{3}{16}\left[u_{i+1,j}h_x\left(\rho_{i,j}h_z + \rho_{i,j-1}h_z^-\right) + u_{i-1,j}h_x^-\left(\rho_{i-1,j}h_z + \rho_{i-1,j-1}h_z^-\right)\right] \\ &+ \frac{3}{16}\left[u_{i,j+1}h_z\left(\rho_{i,j}h_x + \rho_{i-1,j}h_x^-\right) + u_{i,j-1}h_z^-\left(\rho_{i,j-1}h_x + \rho_{i-1,j-1}h_x^-\right)\right] \\ &+ \left.\frac{1}{16}\left(u_{i+1,j+1}\rho_{i,j}h_x h_z + u_{i+1,j-1}\rho_{i,j-1}h_x h_z^- + u_{i-1,j+1}\rho_{i-1,j}h_x^- h_z + u_{i-1,j-1}\rho_{i-1,j-1}h_x^- h_z^-\right)\right\} + O\left(h^3\right), \end{aligned} \quad (19)$$

where h represents the largest of h_x, h_x^-, h_z and h_z^-.

The complete discrete form of (8) can be easily assembled using the formulae presented above; because of the rather large size of the resulting algebraic expression, we will omit it here. The discretized form of the horizontal component of the equation of motion in (8) can be obtained with the same method.

Because of the finite size of our computational grid, we define the following boundary conditions. At the bottom of the model, we assume zero displacement. This condition is appropriate if the model's depth is sufficiently high compared with the loading force wavelength

(the actual minimal depth depends on the model structure and acceptable error level); implementation of this condition is trivial. The left- and right-hand boundaries of the domain can be modelled as either periodic or absorbing boundaries (the latter uses a 1-D version of our finite-difference method to obtain the solution for the vertical profile at the boundary, which is then used as constant boundary condition); the choice between the two options depends of the chosen subsurface model. For the free slip and water pressure boundary conditions, we simply substitute the expressions of boundary conditions (4) and (5) into (8) to obtain a modified form of the FD expressions (14 and 18) for the top row of grid nodes corresponding to the seafloor.

The finite-difference approximations of the equations of motion form a linear system of equations of the form:

$$\sum_{k=-1}^{1}\sum_{l=-1}^{1}(c_{i,j,k,l}u_{i+k,j+l} + d_{i,j,k,l}w_{i+k,j+l}) = b_{i,j}. \tag{20}$$

The resulting coefficient matrix is sparse and symmetric. Although the displacement components u and w are complex, we can solve for real and imaginary parts independently, without recalculating the coefficient matrix, because the coefficients c and d are always real (as follows from the derivation), and only $b_{i,j}$ have both real and imaginary parts, corresponding to the pressure loading function on the seafloor (5).

2.3 Solution methods and implementation

We use a direct solution method to solve the system of linear equations. Another option would be an iterative approach, which is often preferable for large systems because of its relatively small memory requirements. We tested several different methods (with a variety of no-fill preconditioners) on simple models with a homogeneous distribution of material properties of which the best results (fastest convergence) were obtained with D-ILU preconditioned conjugate gradients (CG) and a modified successive over-relaxation (SOR) with successive multigrid refinement (Barrett *et al.* 1994). Whereas the preconditioned CG worked significantly faster, SOR allowed implementation of an exponential decay of displacement as the bottom boundary condition, which significantly reduced the minimum depth requirement. However, for large models containing large-scale features with high material property contrasts (e.g. a melt lens in an otherwise solid or mushy background), none of the iterative methods we tested converged sufficiently fast.

The model software is written in C++ and is cross-platform compatible. All calculations are done in double precision. The current version of the software utilizes CHOLMOD (Chen *et al.* 2006) and UMFPACK (Davis 2004) software packages for sparse matrix factorization and update implementing Cholesky and LU decomposition, respectively.

2.4 Quasi-static and dynamic solutions

An additional advantage of a direct solution method is that one can significantly decrease the computational time if the inertial terms in the governing eq. (8) are ignored (the quasi-static assumption). In this case, the coefficient matrix of our finite-difference problem does not change with changing frequency and the most computationally expensive step in the solution process—the decomposition of the matrix—only needs to be performed once for any number of frequencies/wavelengths. Assuming that we need to calculate compliance for N different frequencies over a given subsurface model, the quasi-static assumption allows us to cut down the computation time almost N-fold, which becomes significant when we need to calculate compliances over and over again (e.g. for inversions or for parameter sensitivity studies).

The quasi-static assumption introduces an error in the amplitude of the compliance signal and also neglects the phase difference between the pressure wave and displacement of the seafloor. Both of these errors depend on the model structure and values of material properties and are insignificant in most cases, but their importance is difficult to predict beforehand. However, we can estimate it using several methods, ranging from direct analysis of the governing eqs (2) or (8) for simple cases (e.g. elastic half-space), to comparing the difference between quasi-static and fully dynamic solutions for select cases. In general, we use the quasi-static assumption when we calculate compliance for a large number of small variations on a model (parameter sensitivity studies), then use non quasi-static calculations to verify the end-members and any interesting aspects of intermediate models. In this paper, we will specifically state where we used the quasi-static solution and report the estimated maximum error associated with its use.

2.5 Quadrature error correction

Since our numerical model is based on second-order finite-difference approximations (11), we can utilize simple 'quadrature error correction' to improve the accuracy of the result. Assuming that the calculated compliance is a sum of true compliance and the error related to finite grid resolution, we can write

$$\eta_h = \eta + Eh^2 + O(h^3), \tag{21}$$

where η is the true compliance, h represents the grid size and η_h is the compliance calculated using the discrete model. The h^2 term can be eliminated by calculating compliance for two models with the same structure and elastic properties but different grid sizes:

$$\eta = \frac{\eta_{h_1}h_2^2 - \eta_{h_2}h_1^2}{h_2^2 - h_1^2}. \tag{22}$$

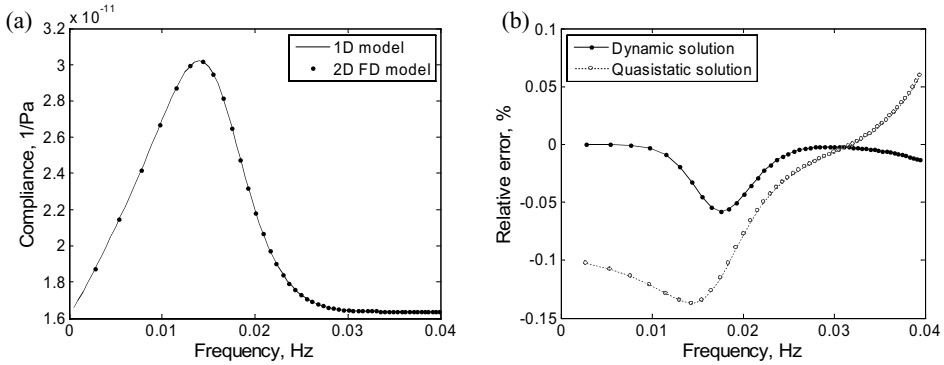

Figure 2. (a) Comparison between compliance calculated using 1-D minor vector method (solid line) and 2-D finite-difference model (dots) for the laterally homogeneous crustal model with a 200 m thick LVZ centred at 1.5 km depth. (b) Relative calculation error of 2-D model compared with the results of the 1-D model for fully dynamic (solid line) and (dashed line) quasi-static solution methods. The limited density of the frequency interval sampling for the finite-difference model in the lower-frequency region is due to the requirements for the periodic lateral boundary conditions.

This simple correction allows us to significantly improve the precision of our calculations with a comparatively small increase in computation time.

2.6 Testing and evaluation

To validate our modelling code, we first calculated compliance for a few simple models for which a reference compliance was determined using established techniques.

Following Crawford *et al.* (1998), we first calculated the compliance for two half-space models with significantly different shear moduli. For the first model, we use material properties typical for oceanic crustal gabbros ($V_P = 7$ km s^{-1}, $V_S = 3.8$ km s^{-1}, $\rho = 3000$ kg m^3), and the second model uses properties consistent with oceanic crust with a small percentage of partial melt ($V_P = 5$ km s^{-1}, $V_S = 1.5$ km s^{-1}, $\rho = 2500$ kg m^{-3}). The model width is 50 km, depth is 75 km, and the water depth is 2000 m. The computational domain size is 1000 × 350 nodes (width × depth), with a constant spacing of 50 m in horizontal direction and the vertical grid spacing increasing exponentially with depth from 10 to 1000 m. The second grid, used for quadrature error correction, has half this resolution (500×175 grid nodes). We calculate compliance for frequencies ranging from 0.00277 to 0.04 Hz and compare the results with reference values obtained using the 1-D code (Crawford *et al.* 1991) and the analytical (quasi-static) formula (Sorrels & Goforth 1973). The calculated compliance is always slightly below the reference values, with error amplitude increasing from 10^{-6} per cent at the lowest frequency to 0.003 per cent at the highest frequency for the gabbroic rock model and from 10^{-5} to 0.09 per cent for the partial model. These errors are, at least, an order of magnitude smaller than that reported for previously published finite-difference compliance models (Crawford *et al.* 1998; Latychev & Edwards 2003). The improvement is due to our more precise finite-difference formulation and utilization of the optimized computational grid, with the vertical cell size generally increasing (decreasing resolution) with increasing depth.

A second test uses a laterally homogeneous crustal model ($V_P = 7$ km s^{-1}, $V_S = 3.8$ km s^{-1}, $\rho = 3000$ kg m^{-3}) containing a 200 m thick low-velocity zones (LVZ; $V_P = 3$ km s^{-1}, $V_S = 150$ m s^{-1}, $\rho = 2500$ kg m^{-3}) centred at 1500 m beneath the seafloor. The contrast between the LVZ and the background material is sharp, with no transition zone or any smoothing applied. Fig. 2 compares the compliance obtained using our FD model with 1000 × 350 grid resolution with the compliance calculated using the 1-D minor vector propagator matrix code (Crawford *et al.* 1991). The difference is below 0.06 per cent for the dynamic solution and below 0.14 per cent for the quasi-static assumption.

Finally, we test our model against the results obtained by Hulme *et al.* (2005) using the quasi-analytical method for 2-D cylindrical bodies. Following the test cases presented by Hulme *et al.* (2005), we calculate compliance for two cases: a mush cylinder (centred 1500 m deep, 600 m radius) and a smaller pure melt cylinder (1500 m deep, 300 m radius). 'Mush' is defined by $V_P = 3.5$ kms^{-1} and $V_S = 1.2$ kms^{-1}, pure melt is assumed to have velocities $V_P = 2.8$ kms^{-1} and $V_S = 1$ m s^{-1} and background material has velocities $V_P = 6$ km s^{-1} and $V_S = 3$ km s^{-1}. The density of all materials is 2700 kg m^{-3}. Water depth is 2700 m.

For the shallow mush cylinder, there is a good match between the results of the two models, with some minor discrepancies (Fig. 3). The finite-difference model shows higher attenuation of the compliance signal with increasing offset, which is likely the result of limited size of the computational domain. The finite-difference model also shows a higher peak compliance signal; however, we believe that in this case, the finite-difference model is more accurate because the quasi-analytical model ignores multiple scattering (Hulme *et al.* 2005). This is partially confirmed by Fig. 3(b), which shows that the difference between the two models is significantly less if the melt cylinder is smaller and, consequently, its top is further from the seabed, resulting in a decreased secondary scattering effect.

3 COMPARISON OF CYLINDRICAL AND ELLIPTICAL MELT BODIES

Since imaged melt bodies at ocean ridges are often much wider than they are tall, the shape factor must be taken into account. In this section, we calculate seafloor compliance over flattened LVZs and compare the results with those obtained for cylindrical bodies.

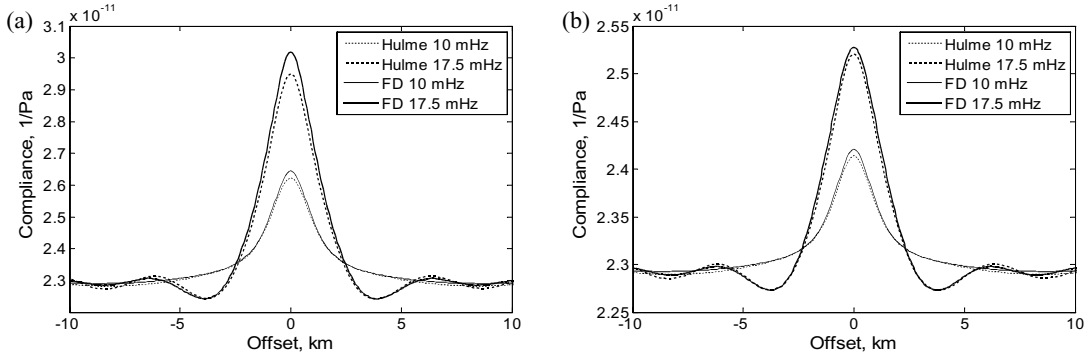

Figure 3. Comparison of the results obtained by 2-D finite-difference (FD) model to those of quasi-analytical model of 2-D cylinders by Hulme *et al.* (2005). (a) 600-m radius mush ($V_P = 3.5$ km s^{-1}, $V_S = 1.2$ km s^{-1}) cylinder and (b) smaller, 300-m radius pure melt ($V_P = 2.8$ km s^{-1}, $V_S = 1$ m s^{-1}) cylinder.

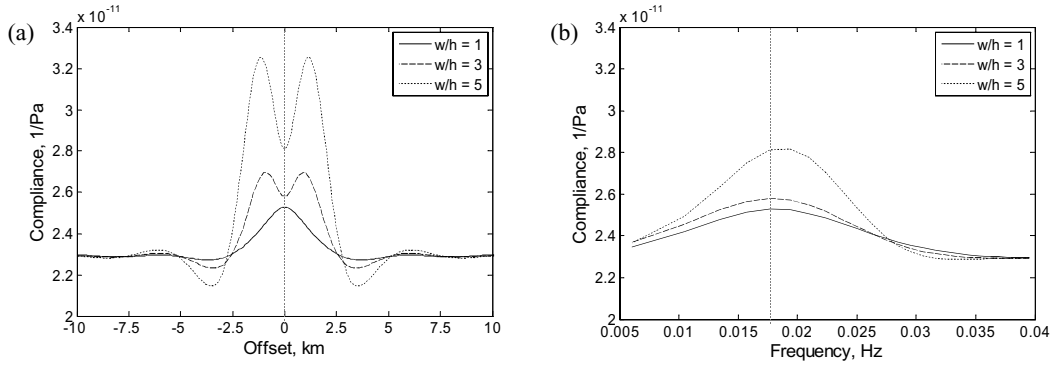

Figure 4. Compliance of pure melt 2-D elliptic bodies for three different width to height ratios. (a) compliance as a function of offset at frequency of 17.6 mHz, (b) compliance as a function of frequency at zero offset (dashed vertical line line shows the frequency used in a).

We model an elliptical LVZ with the major axis oriented horizontally. For the sake of meaningful comparison, we keep the volume of the melt body constant for all shapes considered; each shape is referred to by its ratio of width to height (w/h). We use a range of w/h from 1 (cylinder) to 8; the finite resolution of our model does not allow us to adequately represent the elliptical shape for w/h much higher than 8.

We first present the results for a shallow LVZ, based on a cylinder centred 1500 m deep, having 300 m radius (same as in Section 2, Fig. 3b, except we increased background V_S to a more realistic 3.5 km s^{-1}). For a pure melt LVZ ($V_P = 3$ km s^{-1}, $V_S = 0$ km s^{-1}), flattening significantly increases the compliance signal (Fig. 4). In addition, a double peak is observed in the compliance offset profile within the frequency range corresponding to the peak compliance values (Fig. 4b).

For a mush body ($V_P = 3.5$ km s^{-1} and $V_S = 1.2$ km s^{-1}), the results are drastically different (Fig. 5). Even though the compliance function is nearly identical for 'cylindrical' mush and pure melt bodies—confirming the results obtained by Hulme *et al.* (2005)—compliance hardly increases as the mush body flattens and the double peaks barely develop (Figs 4 and 5). This different behaviour is additionally illustrated by comparing the peak compliance amplitude as a function of ellipse shape for pure melt and mush ellipses (Fig. 6). This result holds for all tested melt zone depths (1.5 and 5.5 km) and sizes (300, 600 and 1200 m radii).

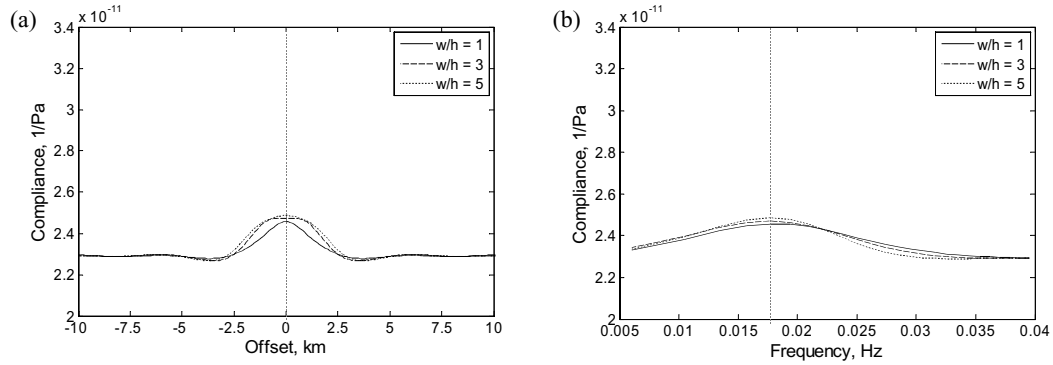

Figure 5. Compliance of 'mush' 2-D elliptic bodies for three different width to height ratios. (a) compliance as a function of offset at frequency of 17.6 mHz and (b) compliance as a function of frequency at zero offset (dashed vertical line shows the frequency used in part a).

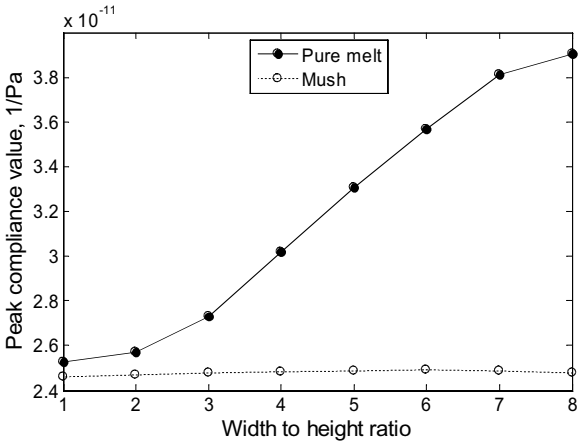

Figure 6. Peak compliance amplitude as a function of ellipse shape for pure melt (solid line) and mush (dashed line) for a shallow melt body (depth to centre 1.5 km, cylinder radius 300 m).

These results indicate that melt 'lenses' will have a much stronger compliance signal than melt 'chambers'. The behaviour of these lenses is much closer to that predicted by 1-D theory than that suggested by scattering theory for a cylindrical geometry. These results also suggest that a flattened pure melt body could be identified by the double peak that it generates, and that this double peak could help to constrain the lens width, as well as creating much sharper lateral variations in compliance signal than previously inferred (Crawford *et al.* 1998, Hulme *et al.* 2005).

4 PARAMETER SENSITIVITY STUDY FOR MELT LENSES

The previous section demonstrated that both the shape and the shear velocity within the melt lens are important factors defining the seafloor compliance. In this section, we look at what size and shape of melt lens can and cannot be seen by compliance measurements. We focus on two cases: 1.5 km and 5.5 km depth to the top of the lens. The former corresponds to the shallow axial melt lenses observed at 9°–10° EPR from seismic reflection/refraction studies (Detrick *et al.* 1987; Kent *et al.* 1993a,b, 2000; Vera & Diebold 1994; Hussenoeder *et al.* 1996, 2002; Collier & Singh 1997; Hooft *et al.* 1997; Tolstoy *et al.* 1997; Singh *et al.* 1998; Tong *et al.* 2002); the latter represents a possible Moho-level melt body (Garmany 1989; Sparks & Parmentier 1994; Barth & Mutter 1996; Crawford *et al.* 1999). We vary the thickness, width and melt fraction within the lens. The parameter sensitivity study presented here is helpful for first-order analysis of more complex cases, such as that presented in the next section of this paper.

The actual structure of a crustal melt lens can be rather complex as not only shape but also the melt fraction can change within the lens (Singh *et al.* 1998). We could model such cases, but a complete parametrization of the range of possibilities is impractical. For this study, we define 'melt lens' as a homogeneous horizontal layer of constant thickness and finite lateral extent. We also assume that the surrounding 'background' material is also homogeneous. Although such simplifications make direct comparison to any real scenario difficult, the obtained results provide important information on the effect of change in the main parameters describing a melt lens on the general structure of the compliance function.

Because of the large number of runs required to test the range of models with various parameters of the melt lenses, the calculations for this study were performed using the quasi-static assumption (see Section 2), which reduces the computational times by more than an order of magnitude. Around 6000 runs used in this test took 10 days on a modern personal computer. The maximum error observed by comparing the quasi-static assumption with the full dynamic solution for several worst-case scenarios (large pure melt lenses) is less than 2 per cent of the peak compliance value, which is less than typical measurement error in mid-ocean ridge compliance data (Crawford & Webb 2002); in most cases, the error is significantly less. We therefore consider the quasi-static results adequate for our generic parameter sensitivity study.

The compliance function for a 2-D model can be rather complex, varying with both frequency and offset. To present the results of the parameter sensitivity study in a compact format, we define several characteristic parameters that describe the compliance function (Fig. 7). The most obvious are 'peak amplitude' and 'peak frequency'; in addition, we calculate the 'central peak amplitude' (the peak compliance directly over the centre of the anomaly) and the corresponding 'central peak frequency'. To define the spatial structure of the compliance function, we define the compliance peak 'half-width' as one-half of the distance between the two farthest extremes that are at one-half of the peak amplitude, and we plot the 'lateral offset' of the compliance peak from the centre of the lens (non-zero only if there are double peaks). Because of the discrete sampling in the frequency domain, dictated by the periodic lateral boundary conditions, the peak frequency values were calculated using a cubic spline interpolation.

Even with just three variable parameters (lens velocity, width and height), the parameter space has too many scenarios to show here—below we only show the cases that have an important effect on the compliance or the interpretation of compliance data. Most of these cases focus on pure melt lenses (which give the highest signals), along with changes in these parameters as a result of increase in lens' shear velocity.

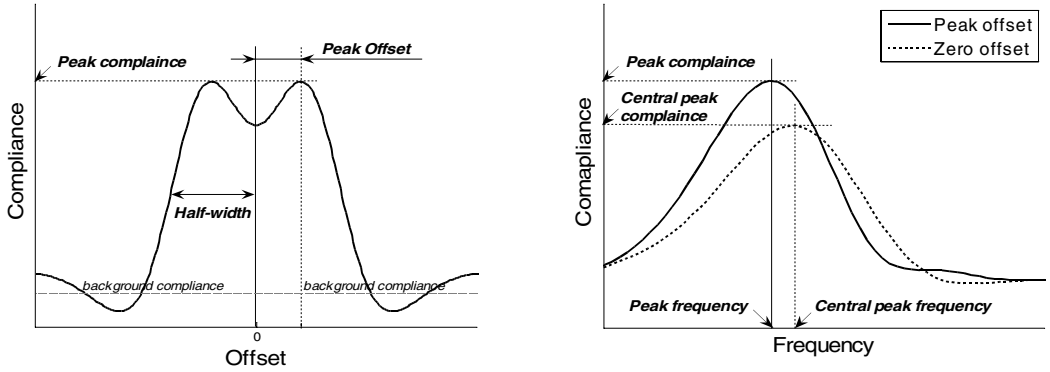

Figure 7. Illustration of parameters used to characterize the compliance signal of a flat melt lens (see text for details).

In all cases, the lens is embedded in the homogeneous material with velocities $V_S = 3.5$ km s^{-1} and $V_P = 6$ km s^{-1}, density for both lens and background material is $\rho = 2700$ kg m^{-3} and water depth is 2700 m.

Fig. 8 demonstrates the effect of changing the width of a pure melt lens ($V_S = 0$ m s^{-1}), on the shape of the compliance function. As expected, the compliance signal increases with increasing lens width (Fig. 8a); the increase is close to exponential even for very large lens widths. Small melt lenses, on the other hand, are unlikely to be identified by compliance measurements, even if composed of pure melt, for example, a 100-m thick pure melt lens ($V_S = 0$ m s^{-1}) will only be detectable by compliance if it is more than 1 km wide, for 5 per cent compliance uncertainty (this result will vary depending of the background velocity structure). We also confirm that the peak frequency of the compliance signal (Fig. 8b) is much higher for finite-size lenses than that predicted by 1-D modelling for layers of infinite extent (Crawford *et al.* 1991, 1998; Hulme *et al.* 2005). 1-D modelling predicts a peak below 10 mHz for a 1.5 km deep melt lens, whereas a finite-extent melt lens less than 4 km wide has a peak frequency between 16 and 19 mHz. For a deep melt lens (5.5 km below the seafloor), 1-D modelling predicts that the peak will be below 6 mHz, whereas it is actually above 7 Hz, if the lens is less than 10 km wide. Geophysical inversions using 1-D forward modelling will therefore underestimate the depth, vertical extent and velocity anomaly in finite low-velocity zones. Finally (Fig. 8c), the spatial extent of the compliance anomaly is significantly wider than the melt lens, unless the lens is much wider than it is deep.

Fig. 9 demonstrates the effect of changing the lens thickness (H) on the compliance signal. For both shallow and deep lenses, the compliance amplitude increases sharply at very small thicknesses (this is only observed for lenses with near-zero shear velocity) and then increases gradually, almost linearly, for larger H (Fig. 9a). The peak frequency changes slightly as the lens thickens, but this change is mostly due to the increasing depth to the bottom of the lens (we kept the depth to top of the lens constant). The width of the compliance peak also changes little (the decrease in peak offset for the deep lens seen in Fig. 9c is the result of a significant change in the lens shape; similar effect was shown in Section 3).

Finally, in Fig. 10, we show the effect of changing shear velocity within the lens. As expected, increasing the shear velocity decreases the compliance amplitude, but this change is much more subtle for very small V_S than that predicted by 1-D models (Crawford *et al.* 1991), especially if the lens is narrower than it is deep (Fig. 10a). The peak compliance frequency decreases as the lens' shear velocity increases (Fig. 10b), which is the opposite of the 1-D case. Finally, the lens shear velocity does not drastically affect the spatial characteristics of the peak (Fig. 10c), with a notable exception being the decrease in peak offset and even disappearance of double peaks at larger shear velocities; we point out, however, that wide LVZs can continue to produce double compliance peaks even for high ($\sim$1.5 km s^{-1}) shear velocities, although the contrast between peak and central compliance amplitudes (Fig. 10a) is less than that for pure melt lenses.

Another very interesting result is that, if we insert a single cell of rigid material in the middle of a wide melt lens, the resulting compliance will be almost as low as for a melt lens half as wide as the original. For example, a shallow pure melt lens 100 m thick and 4 km wide produces peak compliance of 4.2×10^{-11} Pa^{-1}; however, the same lens with a 200 m wide mush region in the middle produces peak compliance of only 3.1×10^{-11} Pa^{-1}, which is about the same as that of a single 2.6 km wide lens (Fig. 8a). This suggests that any solid or 'mushy' part of a melt lens will take up all of the strain, and any melt lens dimensions indicated by compliance measurements would actually be minimum values.

Based on the results presented in this section, we can conclude that the compliance function can be quite complex and very sensitive to a large number of parameters. And although these results cannot be used directly due to simplicity of the chosen models, they will, nevertheless, provide rough guidelines in interpretation of real compliance measurements presented in the following sections.

5 EPR 9°48′N COMPLIANCE DATA FITTING

EPR compliance measurements at 9°48′N (Crawford *et al.* 1999; Crawford & Webb 2002) show several peculiar features, including a narrow-band peak at around 7–8 mHz at two sites within less than 1 km of the rise axis and absent further off-axis (see Fig. 11). Crawford *et al.* (1999) interpreted this peak as indicating a Moho-level melt body. In this section, we attempt to reproduce this peak using our 2-D model. We also look closely at the sensitivity of the compliance measurements to the shallow (1.5 km deep) melt lens. Finally, we evaluate the shear velocities

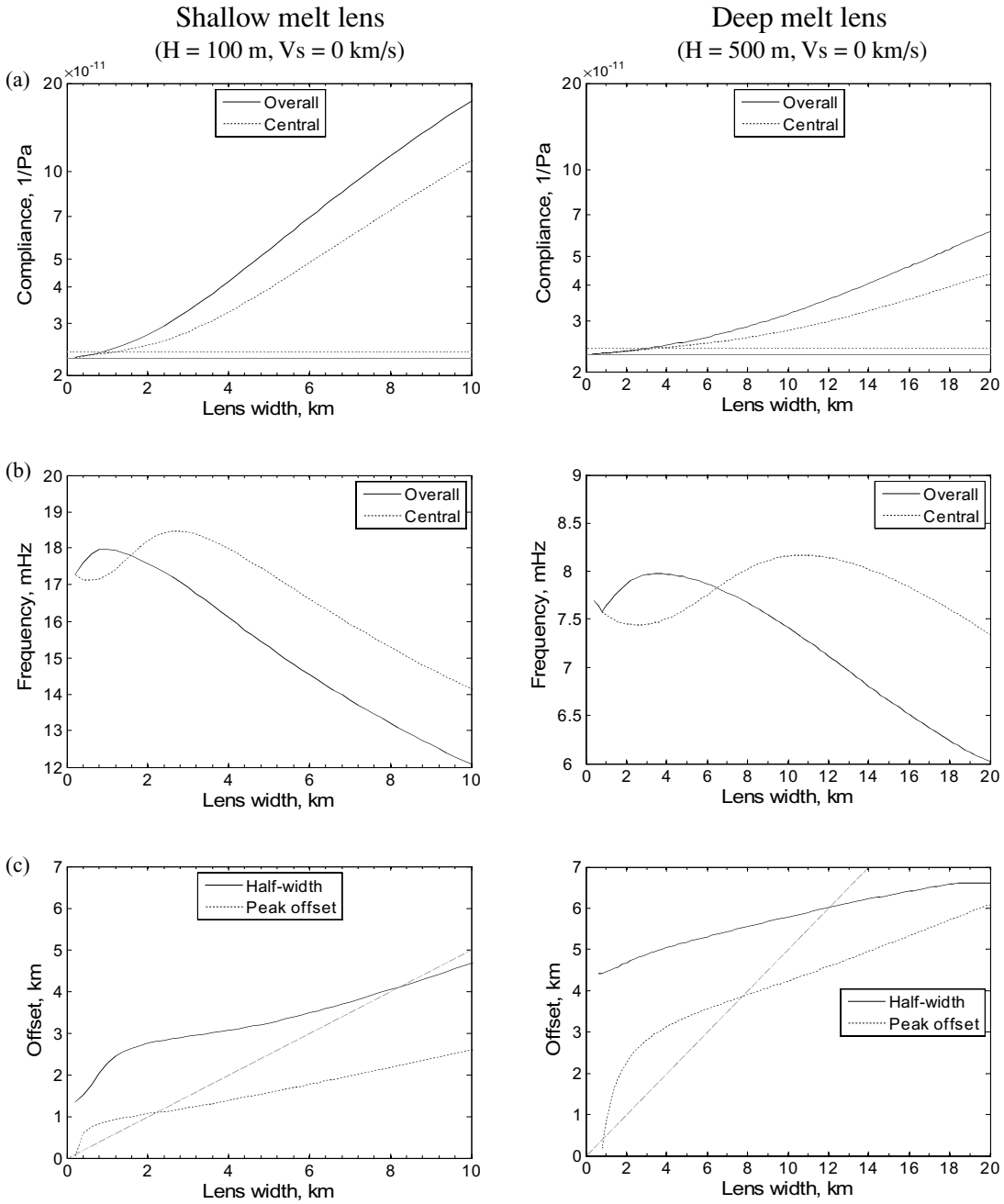

Figure 8. Effect of changing the width of a melt lens on the compliance signal. (a) peak compliance, grey horizontal lines mark base compliance (no lens present, solid line) and 5 per cent increase over it (dotted line); (b) peak frequency and (c) spatial half-width of the compliance peak and lateral offset of the peak from the centre of the lens (grey dashed line indicates the width of a peak corresponding to the width of the lens). The asymptotic behaviour of the half-width of a deep melt lens for high lens widths is the result of the finite lateral size of the model used in simulations (50 km).

in the lower crustal mush zone estimated by Crawford & Webb (2002). To do so, we perform a series of forward modelling simulations with various melt lens configurations. We use the quasi-static assumption in the initial search for best fitting values but calculated the final results using the fully dynamic solution.

We started with the seismic velocity model constructed linear interpolation of the results by Crawford & Webb (2002), based on 1-D inversions of EPR compliance measurements at 9°48′N and seismic profiles from Dunn *et al.* (2000). For more details on construction of these models, we would like to refer the reader to the aforementioned work of Crawford & Webb (2002), as well as previous work by Crawford *et al.* (1999). Using our 2-D code, this velocity model significantly underestimates compliance at on- and near-axis sites (Fig. 12) and does not produce the localized low-frequency peak.

Since the interpretation of EPR compliance data could require sharply defined zones with near-zero shear velocities (Kent *et al.* 1990; Hussenoeder *et al.* 1996; Crawford & Webb 2002), we kept the model resolution high (1000 × 600, 50 m horizontal grid spacing and variable

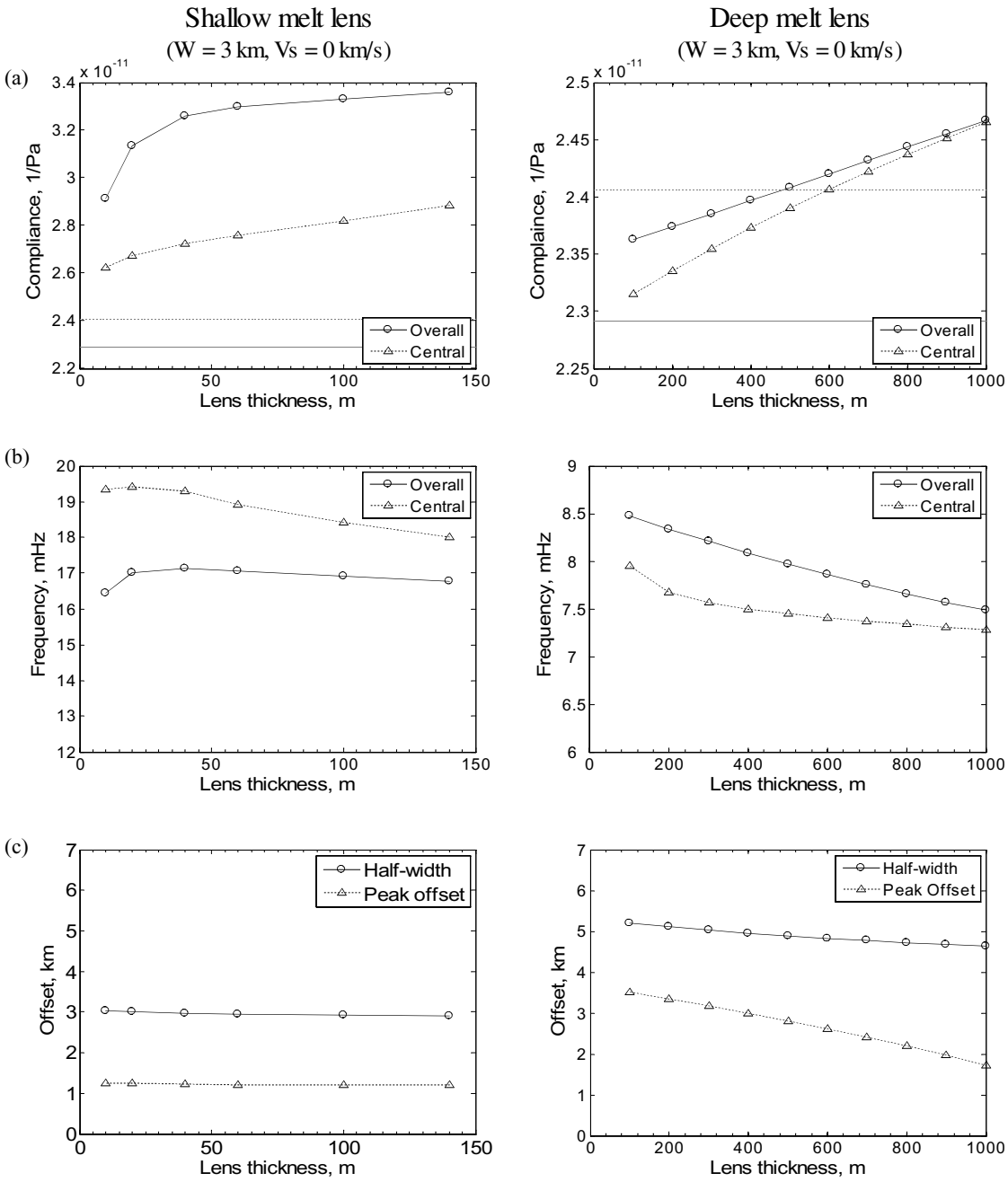

Figure 9. Effect of changing the thickness of a melt lens on the compliance signal. (a) peak compliance, grey horizontal lines mark base compliance (no lens present, solid line) and 5 per cent increase over it (dotted line); (b) peak frequency and (c) spatial half-width of the compliance peak and lateral offset of the peak from the centre of the lens.

vertical grid spacing—starting from 2.5 m in the LVZs—for quasi-static solutions and 500 × 600 for dynamic solution). Unfortunately, even using the quasi-static assumption, the 2-D finite-difference code is too computationally expensive at this resolution (2–3 min per run) to be effectively used in a detailed inverse solution with the available computational resources. Therefore, we cannot yet reliably calculate the subsurface velocity structure including both isolated melt bodies and a background velocity structure from the existing compliance measurements.

We instead built a new starting velocity model without melt lenses, which roughly mimics the spatial and spectral properties of the EPR compliance data, by empirically fitting the data and model structure. To achieve a reasonable spatial representation of the EPR compliance data, we had to decrease the width of the middle crustal low-velocity zone (Crawford & Webb 2002, pp. 122, fig. 6) to only 3 km—which is less than half of that obtained with 1-D inversion (Crawford & Webb 2002) and even narrower than the results of seismic imaging (Dunn *et al.* 2000)—and decrease its shear velocity from 1700 (Crawford & Webb 2002, pp. 121, fig. 4) to just 700 m s^{-1}. The resulting model produces

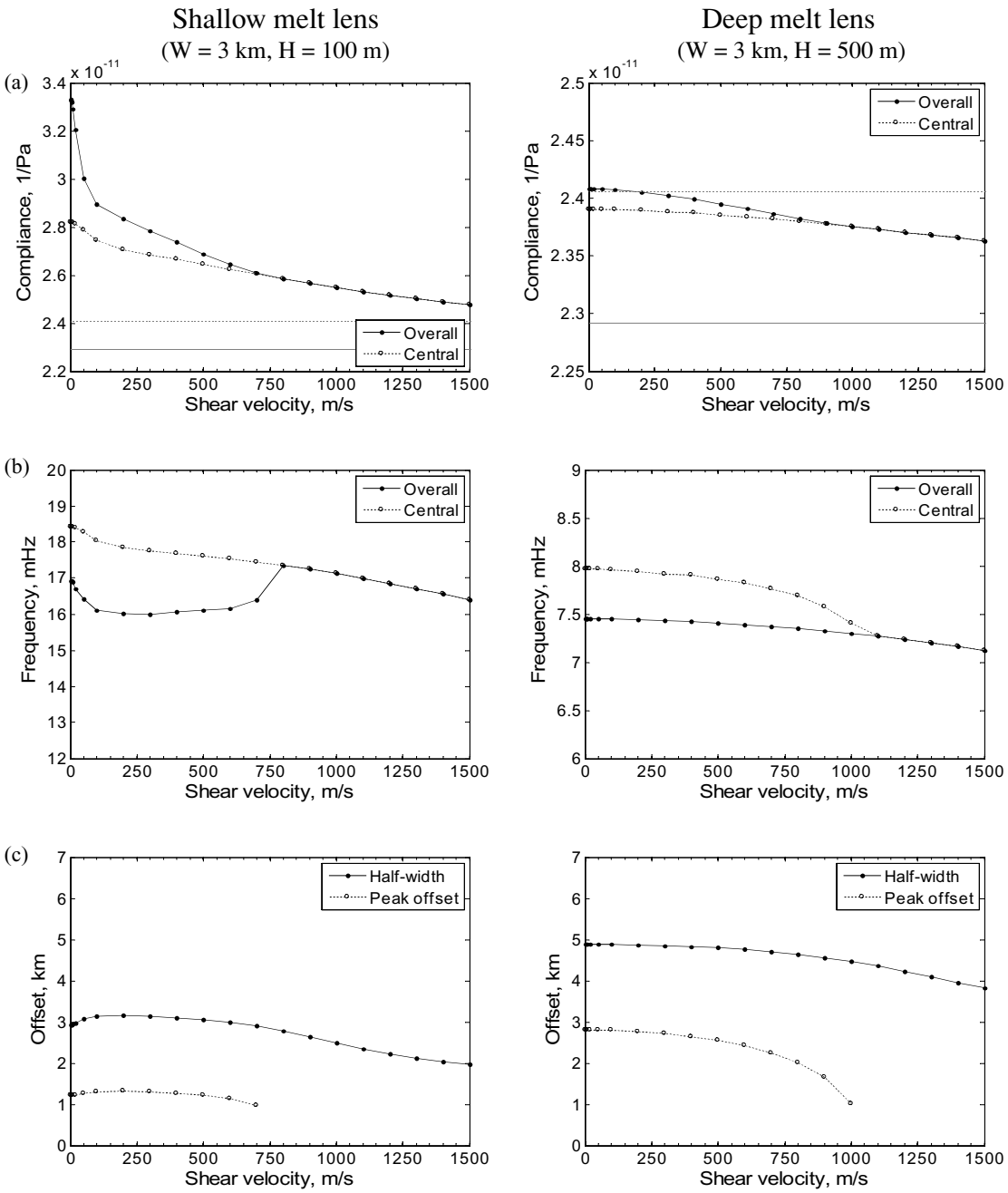

Figure 10. Effect of changing the shear velocity of a melt lens on the compliance signal. (a) peak compliance, grey horizontal lines mark base compliance (no lens present, solid line) and 5 per cent increase over it (dotted line); (b) peak frequency and (c) spatial half-width of the compliance peak and lateral offset of the peak from the centre of the lens.

the compliance illustrated in Fig. 13. Please note that this is an *ad hoc* best fit solution and not necessarily the unique solution, but we could not find a model with shear velocities of 1500 m s^{-1} or more in the lower crustal magma chamber that came close to fitting the data.

We then ran a series of simulations for the shallow (1.5 km deep) and deep melt lenses, varying position, thickness, width and melt content (shear velocity). We used the same simplified lens geometry as that described in Section 4. We quickly found that an 80 m thick (Kent *et al.* 1990) pure melt lens will remain undetectable (signal less than 2 per cent above background) if it is less than 1200 m wide. Assuming the same thickness and compliance sensitivity, a mush lens ($V_S = 1200$ m s^{-1}) less than 3 km wide would be undetectable. Seismic refraction studies (Kent *et al.* 1993a, b) indicate that the shallow melt lens at 9°48′ EPR is only about 500 m wide; so, it would produce an increase in compliance signal well below the measurement error, even under best circumstances. We therefore discarded the presence of the shallow melt lens in our subsequent models.

This test, along with the results presented in the previous section, clearly shows that the compliance method is much more sensitive to a large low-velocity region (such as the EPR lower crustal 'magma chamber') than to a small region of pure melt (such as the EPR mid-crustal

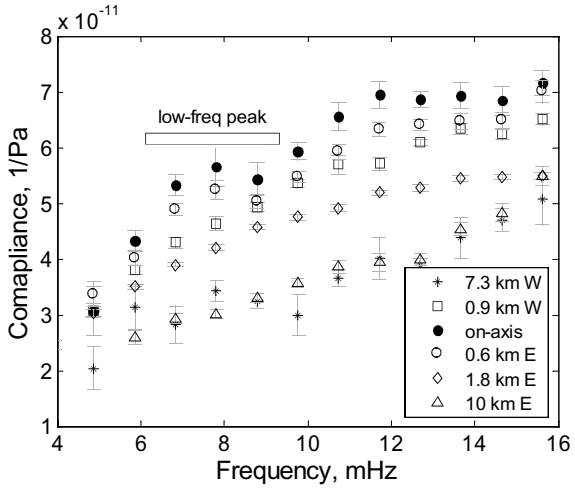

Figure 11. Compliance at select site at EPR 9°48′N as a function frequency for several sites identified by their offsets.

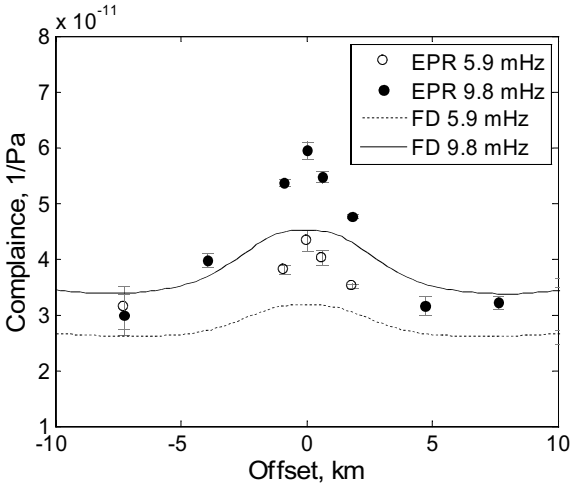

Figure 12. Comparison of the compliance calculated using 2-D finite-difference model for the velocity structure obtained by Crawford & Webb (2002) using 1-D inversion (lines) and the original EPR measurements at the corresponding frequencies (circles with error bars).

melt lens). For a melt lens to be detected by compliance, it must be of pure melt and larger than most of the EPR melt bodies imaged by seismic reflection. Deeper than the shallow melt lens, an even larger body would be needed to be detected by compliance.

While attempting to find a configuration of deep melt lens that would fit the data, we immediately faced several problems. First, our previous results (see Section 4) show that, just as with shallow melt lenses, the compliance peak of a deep melt lens occurs at a frequency

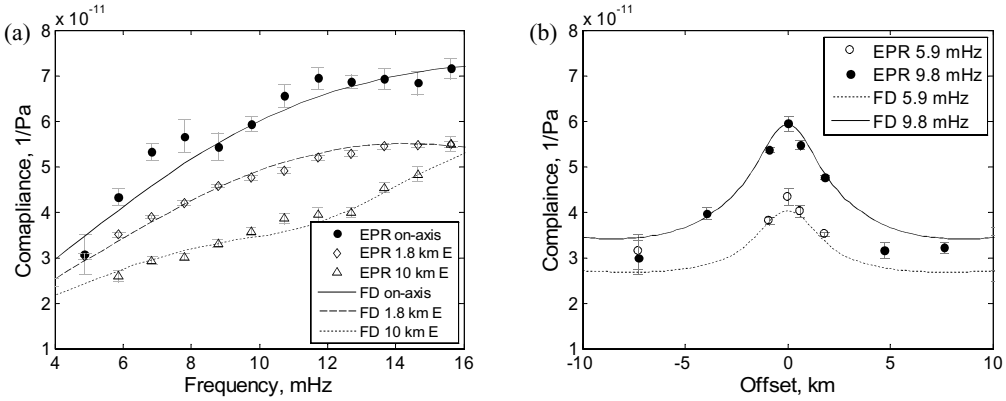

Figure 13. Compliance of the adjusted model of the EPR velocity profile compared with EPR compliance measurements. (a) frequency profile for select offsets and (b) offset profile plotted for select frequencies.

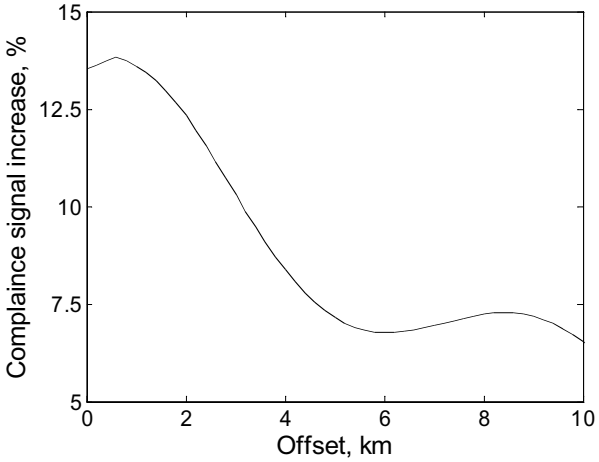

Figure 14. Increase in the 8 mHz compliance signal as a result of introducing a wide, axially centred Moho-depth LVZ to the adjusted EPR velocity model, plotted versus the distance from the rise axis. The LVZ is 20 km wide, 500 km thick, composed of mush ($V_S = 1.2$ km s^{-1}) and its top is 5.5 km below the seafloor.

which increases as the lens width decreases (Fig. 8b). Therefore, if we assume that the low-frequency peak evident in on-axis EPR compliance measurements (Fig. 11) is caused by a Moho-level LVZ centred on the rise axis, the lens must be extremely wide, in excess of 20 km. Such wide LVZ, however, would be evident at very long distances away from the rise axis (Fig. 8c), seemingly contradicting EPR data, where the low-frequency peak is observed only at distances less than 800 m from the rise axis.

One could assume that the spatial localization of the peak may be caused by the narrow low-velocity zone in the middle crust, below the rise, but the simulation results prove otherwise, as can be seen in Fig. 14, which shows change in compliance function of our EPR velocity model as a result of introduction of a Moho-level mush lens (pure melt could not be used because of the limited resolution of the model). A 20 km wide, 500 m thick lens produces an increase in the 8 mHz compliance signal at the rise axis comparable to that observed in low-frequency peak in the EPR compliance data (Fig. 11), but this peak can be observed clearly up to at least 5 km off the rise axis. We tested a variety of other scenarios, including different shapes of the mid-crustal melt zone and narrow vertical zones of low shear strength, but none resulted in a significant decrease of the spatial width of the compliance peak produced by a deep LVZ. Thus, the Moho-level melt sill, if the on-axis compliance anomaly is indeed produced by one, must be narrower and therefore offset from the centre of the ridge.

We ran a series of simulations with a melt sill varying in size from 4 to 20 km in width and various offsets from the centre of the ridge, but none of the configurations tested reproduced the localized low-frequency compliance peak evident in Fig. 11. In all cases, the produced peak was spatially wide, just as predicted in Section 4, which is not surprising, considering that the wavelength of the pressure oscillations corresponding to a 8 mHz compliance signal is 17.5 km (for an approximately 2.5 km water depth). Similarly, the compliance signal of a lens was always broad in the frequency domain. For the peak to be localized below 10 mHz (less than 2 per cent increase in compliance at 10 mHz and above and 10–15 per cent increase at 8 mHz), the lens has to be 8–10 km wide, centred 7–9 km off the rise axis; introduction of such a lens in the model (Fig. 15), while providing a reasonable fit for the on-axis and eastward EPR measurement site, significantly overestimated compliance in the low frequency region of the most westward sites and produced a large increase in the compliance signal below 6 mHz, which is not observed in the EPR data. These misfits could not be compensated for by increasing lower crustal velocities up to $V_S = 3$ km s^{-1} or by increasing mantle V_S to 5 km s^{-1}.

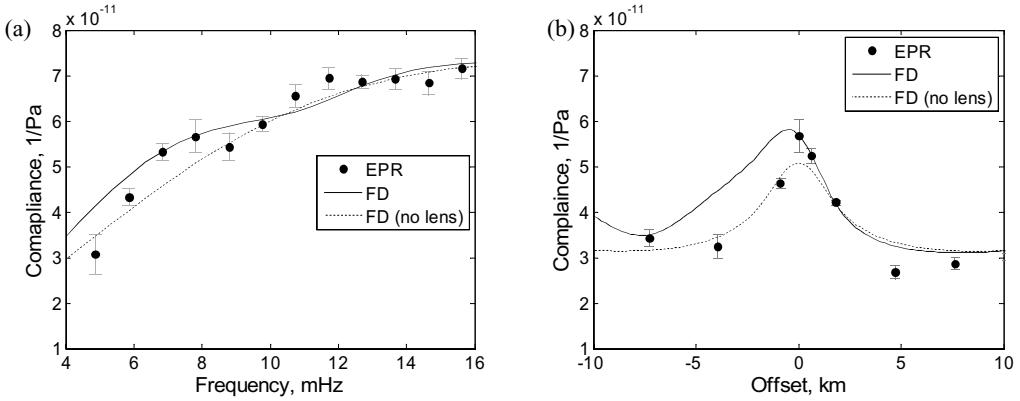

Figure 15. Effect of introducing a 10 km wide 40 m thick Moho-depth pure melt lens centred 8 km west of the rise axis on the compliance of the adjusted EPR velocity model. (a) frequency profile for the on-axis site and (b) offset profile plotted for the 7.8 mHz frequency.

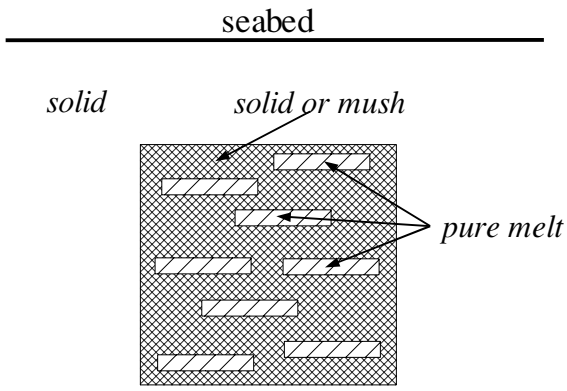

Figure 16. Scematic illustration of the melt distribution used in the experiment. See text for details.

Although we could not match the narrow-band, low-frequency compliance peak evident in the EPR on-axis compliance measurements at 9°48′ with our deep melt lens model, we cannot exclude the existence of a Moho-level LVZ. Similar low-frequency peaks appear in several compliance measurements at different sites along the EPR (Crawford 2002)—ruling out the possibility that this is just an outlier caused by a measurement error or a single event not accounted for, in data processing—and these sites are correlated with mantle low-velocity zones detected by active seismics (Toomey *et al.*, 2007). There may be 3-D effects or more complicated melt structures that we have not yet modelled. Alternatively, the correlation with seismic data could be fortuitous and an entirely different, localized low-frequency process (water circulation, currents, strain adjustment, etc.) could generate the observed low-frequency peak. The raw data should be re-analysed to localize the source of this peak and determine if it changes with time.

6 THE 'EQUIVALENT VELOCITY' OF A ZONE CONTAINING SEVERAL SMALL MELT SILLS

Geochemical and structural studies of the Oman ophiolite (Boudier & Nicolas 1996; Kelemen *et al.* 1997; Korenaga & Kelemen 1997) indicate that the lower crust at fast-spreading ridges may contain one or several melt sills. If these sills are individually too small to be resolved by compliance measurements, several such sills could still affect seafloor compliance, and it is conceivable that the lower crustal 'mush' zone would actually be a large number of isolated sills. To determine if melt sills could generate the compliance signal measured at the EPR, we calculated seafloor compliance over a zone of randomly scattered pure melt bodies in a homogeneous background (Fig. 16). We created a 4-km wide zone from 1.5 to 5.5 km below the seafloor. We embedded isolated pure melt bodies in solid ($V_S = 4.0$ km s^{-1}) or mushy ($V_S = 1.2$ km s^{-1}) material, assuming for each run that all of the melt bodies had the same size and shape. We iterated over different total melt percentages (up to 40 per cent), body sizes and body shapes, varying lens' thickness from 20 to 160 m and lens' width from 20 to 1280 m. We also calculated compliance for uniform low-velocity zones of the same size and with a broad range of velocities. We then matched compliances between the melt lens-filled and uniform zones to determine the 'effective velocity' of the melt lens-filled zones.

Fig. 17 shows the results for melt bodies embedded in solid and mush backgrounds. Melt bodies of different size but the same shape give similar results; so, we grouped them together on the plots. The smallest effect comes from square melt bodies, which only bring the apparent velocity down to half the background velocity at the highest (40 per cent) melt fractions. The compliance signal increases as the bodies become more elongated, either in the vertical or in the horizontal direction. In fact, vertically elongated melt bodies generate a lower

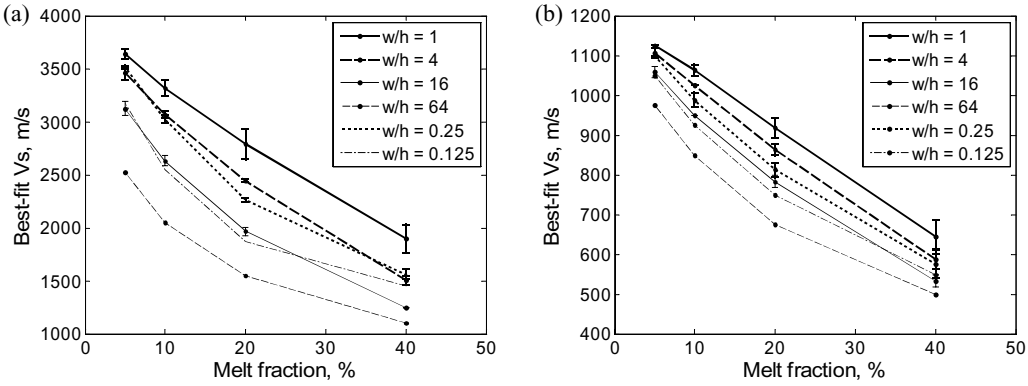

Figure 17. Best-fit equivalent velocity for various melt lens shapes (width/height ratios), plotted against total melt fraction. (a) solid background material ($V_S = 4$ km s^{-1}) and (b) mush background material ($V_S = 1.2$ km s^{-1})

apparent velocity than horizontally elongated melt bodies with the same shape. This is different from the case for isolated bodies, where 'flat' bodies generate a much stronger signal than 'tall' bodies. It appears that a zone of multiple vertical bodies breaks up the resistance of the crust to vertical shearing, whereas flat bodies individually flex under pressure forcing.

Even when melt bodies are elongated, a very large melt percentage would be required to reduce an otherwise solid lower crust to the measured compliance values. Our on-axis estimate of 0.7 km s^{-1} is not obtained even by a 40 per cent volume percentage of melt in sills, with shape factors up to 64. Even putting sills into a mushy (1.2 km s^{-1}) background requires 20 per cent or more volume percent of fluid sills to attain 0.7 km s^{-1}. This does not mean that there are no lower crustal sills, it simply means that there is mush and that most, if not all, of the compliance signal comes from this mush.

7 CONCLUSIONS

Our new 2-D finite-difference compliance modelling algorithm presents several advantages over the existing 2-D algorithm (Crawford *et al.* 1998), including the ability to handle any gridded subsurface structure, with no limitations on the gradients of the material properties, and significantly improved performance with lower memory requirements. 2-D modelling of complex compliance data remains computationally expensive, and there are several factors not yet considered in our model, such as surface topography and the effect of the forcing wave direction. Both may play a role even if the subsurface can be reasonably approximated by 2-D structure. Preliminary studies using waves crossing an EPR model at different angles indicate that compliance may be significantly more sensitive to elongated melt bodies if the waves propagate along the body; so, a continuous pure melt lens along the rise axis might be more easily detected by compliance than indicated by this study, if the forcing waves are travelling along axis. Finally, variations of the subsurface structure in the third dimension may bring even more complexity to the task of interpreting compliance data. All these questions require further development of the model, in particular towards full 3-D implementation, which in turn requires improvements in the computational efficiency of the numerical methods used.

Applying this model to some of the problems inaccessible to previously existing methods (Crawford *et al.* 1991, 1998; Hulme *et al.* 2005) demonstrates that lateral variations in subsurface structure must be accounted for, to adequately interpret compliance data. In areas with significant lateral variations, the utilization of 1-D modelling and inversion is likely to result in high interpretation errors, even when additional subsurface structure information is available. For example, even if we know the form of a subsurface low-velocity zone from active seismic data, one cannot accurately calculate its shear velocity using 1-D methods. We find that flattened pure melt bodies have a significantly higher compliance than cylindrical melt bodies with the same cross-sectional area. The compliance created by such bodies often has side peaks over their edges, which are as strong as or stronger than the central peak, requiring a series of measurements to best constrain their size and shear velocity. We also find that melt bodies, the size of those imaged seismically on the EPR, will have little or no effect on the measured compliance. A pure melt body 80 m thick, must be over 1200 m wide to generate a measurable (2 per cent above background) signal. And a mush body ($V_S = 1.2$ km s^{-1}) of the same height would have to be over 3000 m wide to be detected.

We were not able to create a deep melt body that duplicates the tight, low frequency peak observed at several EPR sites and interpreted as a Moho melt body (Crawford & Webb 2002). More work must be done on both modelling and data analysis, before these features can be adequately explained. Finally, we find that the compliance data are far and away most sensitive to the broad, thick, lower crustal partial melt zone. Our simple data fitting model required shear velocities as low as 700 m s^{-1} in the centre of this zone, far below the values previously estimated using 1-D model-based inversions and suggesting higher melt percentages than those previously estimated. A full analysis/inversion of these data will be needed to properly constrain these velocities and the range of possible melt percentages.

ACKNOWLEDGMENTS

The authors would like to thank Konstantin Latychev, Spahr Webb and Ralph Stephen for their help in improving the manuscript.

REFERENCES

Aki, K. & Richards, P.G., 1980. *Quantitative Seismology: Theory and Methods*, 932 p., W.H. Freeman and Company, San Francisco, CA.

Barrett, R. *et al.,* 1994. *Templates for the Solution of Linear Systems: Building Blocks for Iterative Methods*, 2nd edn, SIAM, Philadelphia, PA.

Barth, G.A. & Mutter, J.C., 1996. Variability in oceanic crustal thickness and structure: multichannel seismic reflection results from the northern east pacific rise, *J. geophys. Res.,* **101**(B8), 17 951–17 975.

Boudier, F. & Nicolas, A., 1996. Magma chambers in the Oman Ophiolite; fed from the top and bottom, *Earth planet. Sci. Lett.,* **144,** 239–250.

Buck, W.R., Carbotte, S.M. & Mutter, C., 1997. Controls on extrusion at mid-ocean ridges, *Geology,* **25,** 935–938.

Cannat, M., 1996. How thick is the magmatic crust at slow spreading oceanic ridges? *J. geophys. Res.,* **101,** 2847–2857.

Chen, Y., Davis, T.A., Hager, W.W. & Rajamanickam, S., 2006. Algorithm 8xx: CHOLMOD, supernodal sparse Cholesky factorization and update/downdate, Technical Report No. TR-2006-005, University of Florida, available at http://www.cise.ufl.edu/research/sparse/cholmod/.

Collier, J.S. & Singh, S.C., 1997. Detailed structure of the top of the melt body beneath the East Pacific Rise at 9 40N from waveform inversion of seismic reflection data, *J. geophys. Res.,* **102,** 20 287–20 304.

Crawford, W.C., 1994. Determination of oceanic crustal shear velocity structure from seafloor compliance measurements, *PhD thesis*. University of California, San Diego.

Crawford, W.C., 2002. The sensitivity of seafloor compliance measurements to sub-basalt reservoirs, *Lithos Sci. Rep.,* **4,** 139–147.

Crawford, W.C. & Singh, S.C., 2006. Sediment shear velocities in the Faeroe-Shetland Basin from seafloor compliance measurements, *Lithos Sci. Rep.,* **8,** 107–112.

Crawford, W.C. & Webb, S.C., 2002. Variations in the distribution of magma in the lower crust and at the Moho beneath the East Pacific Rise at 9–10°N, *Earth planet Sci. Lett.* **203,** 117–130.

Crawford, W.C., Webb, S.C. & Hildebrand, J.A., 1991. Seafloor compliance observed by long-period pressure and displacement measurements, *J. geophys. Res.,* **96,** 16 151–16 160.

Crawford, W.C., Webb, S.C. & Hildebrand, J.A., 1998. Estimating shear velocities in the oceanic crust from compliance measurements by two-dimensional finite difference modeling, *J. geophys. Res.,* **103,** 9895–9916.

Crawford, W.C., Webb, S.C. & Hildebrand, J.A., 1999. Constraints on melt in the lower crust and Moho at the East Pacific Rise, 9°48′N, using seafloor compliance measurements, *J. geophys. Res.,* **104,** 2923–2939.

Davis, T.A., 2004. Algorithm 832: UMFPACK V4.3, an unsymmetric-pattern multifrontal method with a column pre-ordering strategy, *ACM, Trans. Math. Software,* **30**(2), 196–199, available at http://www.cise.ufl.edu/research/sparse/umfpack/.

Detrick, R.S., Buhl, P., Vera, E., Mutter, J., Orcutt, J., Madsen, J. & Brocher, T., 1987. Multichannel seismic imaging of a crustal magma chamber along the East Pacific Rise between 9°N and 13°N, *Nature,* **326,** 35–41.

Dunn, R.A., Toomey, D.R. & Solomon, S.C., 2000. Three-dimensional seismic structure and physical properties of the crust and shallow mantle beneath the East Pacific Rise at 9 degrees 30′N, *J. geophys. Res.,* **105,** 23 537–23 555.

Garmany, J., 1989. Accumulations of melt at the base of young oceanic crust, *Nature,* **340,** 628–632.

Gomberg, J.S. & Masters, T.G., 1988. Waveform modeling using locked-mode synthetic and differential seismograms: application to determination of the structure of Mexico, *Geophys. J.,* **94,** 193–218.

Hooft, E.E.E., Detrick, R.S. & Kent, G.M., 1997. Seismic structure and indicators of magma budget along the southern east pacific rise, *J. geophys. Res.,* **102,** 27 319–27 340.

Hulme, T., Ricolleau, A., Bazin, S., Crawford, W.C. & Singh, S.C., 2003. Shear wave structure from joint analysis of seismic and seafloor compliance data, *Geophys. J. Int.,* **155,** 514–520.

Hulme, T., Crawford, W.C. & Singh, S.C., 2005. The sensitivity of seafloor compliance to two-dimensional low-velocity anomalies, *Geophys. J. Int.,* **163,** 547–558.

Hussenoeder, S.A., Collins, J.A., Kent, G.M., Detrik, R.S., Harding, A.J., 1996. Seismic analysis of the axial magma chamber reflector along the southern East Pacific Rise from conventional reflection profiling, *J. geophys. Res.,* **101,** 22 087–22 105.

Hussenoeder, S.A., Detrick, R.S., Kent, G.M., Schouten, H. & Harding, A.J., 2002. Fine-scale seismic structure of young upper crust at 17°20′S on the fast spreading East Pacific Rise, *J. geophys. Res.,* **107**(B8), 2156, doi:10.1029/2001JB001691.

Kelemen, P.B., Koga, K. & Shimizu, N., 1997. Geochemistry of gabbro sills in the crust-mantle transition zone of the Oman Ophiolite; implications for the origin of the oceanic lower crust, *Earth planet. Sci. Lett.,* **146,** 475–488.

Kent, G.M., Harding, A.J. & Orcutt, J.A., 1990. Evidence for a smaller magma chamber beneath the east pacific rise at 9°30′N, *Nature,* **344,** 650–653.

Kent, G.M., Harding, A.J. & Orcutt, J.A., 1993a, Distribution of magma beneath the East Pacific Rise between the Clipperton Transform and the 9°17′PN deval from forward modeling of common depth point data, *J. geophys. Res.,* **98,** 13 945–13 969.

Kent, G.M., Harding, A.J. & Orcutt, J.A., 1993b, Distribution of magma beneath the East Pacific Rise near the 9°03′PN overlapping spreading center from forward modeling of common depth point data, *J. geophys. Res.,* **98,**13 971–13 995.

Kent, G.M. *et al.,* 2000. Evidence from three-dimensional seismic reflectivity images for enhanced melt supply beneath mid-ocean-ridge discontinuities, *Nature,* **406,** 614–618.

Korenaga, J. & Kelemen, P.B., 1997. Origin of gabbro sills in the Moho transition zone of the Oman ophiolite: implications for magma transport in the oceanic lower crust, *J. geophys. Res.,* **102,** 27 729–27 749.

Latychev, K. & Edwards, R.N., 2003. On the compliance method and the assessment of three dimensional sea floor gas hydrate deposits, *Geophys. J. Int.,* **155,** 923–952.

Phipps Morgan, J., 1987. Melt migration beneath mid-ocean spreading centers, *Geophys. Res. Lett.,* **14,** 1238–1241.

Singh, S.C., Kent, G.M., Collier, J.S. & Harding, A.J., 1998. Orcutt, Melt to mush variations in crustal magma properties along the ridge crest at the southern East Pacific Rise, *Nature,* **394,** 874–878.

Smith, D.K. & Cann, J.R., 1993. Building the crust at the mid-atlantic ridge, *Nature,* **365,** 707–715.

Sorrels, G.G. & Goforth, T.T., 1973. Low frequency earth motion generated by slowly propagating, partially organized pressure fields, *Bull. seism. Soc. Am.* **63,** 1583–1601.

Sparks, D.W. & Parmentier, E.M., 1994. The generation and migration of partial melt in the mantle, in *Magma Transport,* pp. 55–76, ed. Ryan, M.P., Academic Press Inc. New York.

Tolstoy, M., Harding, A.J. & Orcutt, J.A., 1997. Deepening of the axial magma chamber toward the garret fracture zone from multichannel data, *J. geophys. Res.,* **102,** 3097–3108.

Toomey, D.R., Jousselin, D., Dunn, R.A., Wilcock, W.S.D. & Detrick, R.S., 2007. Skew of mantle upwelling beneath the East Pacific Rise Governs Segmentation, *Nature,* **444,** 409–414, doi:10.1038/nature 05679.

Tong, C.H. *et al.,* 2002. Asymmetric melt sills and upper-crustal construction beneath overlapping ridge segments: implications for the development of melt sills and ridge crests, *Geology,* **30**(1), 83–86.

Trevorrow, M.V. & Yamamoto, T., 1991. Summary of marine sedimentary shear modulus and acoustic speed profile results using a gravity wave inversion technique, *J. acoust. Soc. Am.,* **90,** 441–456.

Vera, E.E. & Diebold, J.B., 1994. Seismic imaging of oceanic layer 2A between 9°30′N and 10°N on the east pacific rise from two-ship wide aperture profiles, *J. geophys. Res.,* **99**(B2), 3031–3041.

Willoughby, E.C. & Edwards, R.N., 1997. On the resource evaluation of marine gas-hydrate deposits using seafloor compliance methods, *Geophys. J. Int.,* **131,** 751–766.

Willoughby, E.C. & Edwards, R.N., 2000. Shear velocities in Cascadia from seafloor compliance measurements, *Geophys. Res. Lett.,* **27,** 1021–1024.

Yamamoto, T. & Torii, T., 1986. Seabed shear modulus profile inversion using surface gravity (water) wave-induced bottom motion, *Geophys. J. R. astr. Soc.,* **85,** 413–431.

Yamamoto, T., Trevorrow, M.V., Badiey, M. & Turgut, A., 1989. Determination of the seabed porosity and shear modulus profiles using a gravity wave inversion, *Geophys. J. Int.,* **98,** 173–182.